Turbulence statistics in rotating channel flows with rough walls

Wen Wu[1]

Department of Mechanical Engineering
Johns Hopkins University, Baltimore, MD, USA

Ugo Piomelli[2]

Department of Mechanical and Materials Engineering
Queen's University, Kingston, Ontario, K7L 3N6, Canada

Junlin Yuan[3]

Department of Mechanical Engineering
Michigan State University, East Lansing, MI, USA

Abstract

We performed direct simulations of channel flow subjected to rotation about a spanwise axis, comparing cases with smooth and rough walls. The destabilizing effect of roughness counteracts the stabilizing effect of rotation on the cyclonic (stable) side. When the surface is rough the Reynolds stresses remain significant at all rotation rates considered, even those that results in a quasi-laminar state when the wall is smooth. The wake fluctuations result in significant dispersive stresses, which give an important contribution to the generation of turbulence on the stable side, mainly through added production of shear stresses. The dispersive stresses are mostly associated with the channeling of the flow between roughness elements.

Keywords: Large-eddy simulations, turbulent boundary layers, roughness, rotation

---

1. Introduction

Wall-bounded flows subjected to rotation around the spanwise axis occur in a number of applications, the most common one being turbomachinery. In a rotating frame of reference the Coriolis force, $\mathbf{\Omega} \times \mathbf{V}$ appears in the equations of motion. Here, $\mathbf{\Omega}$ is the rotation rate and $\mathbf{V}$ the fluid velocity. The Coriolis term

---

[1] Email: wenwu.cfd@gmail.com.
[2] Email: ugo@queensu.ca.
[3] Email: junlin@egr.msu.edu.

can stabilize or destabilize the flow, depending on the value of the dimensionless rotation number ($Ro = 2\Omega/S$, where S is the mean shear), and on whether Ro and S have the same sign (see Durbin and Pettersson Reif (2011) for an extended discussion).

In a plane channel the mean shear has opposite signs on the two sides. For positive Ro, then, the lower wall (the pressure side) is subjected to anti-cyclonic rotation (since Ro and S have the same sign) and the flow is may be either stabilized or de-stabilized, depending on the rotation rate. On the upper, suction, side the rotation is cyclonic and the flow is always stabilized.

This flow has been studied extensively. Johnston et al. (1972) reported the first velocity and Reynolds stress measurements in rotating channel, and Kristoffersen and Andersson (1993) carried out the first numerical simulation of this problem. Other studies of this flow include the work by Tafti and Vanka (1991); Lamballais et al. (1996); Nakabayashi and Kitoh (1996, 2005); Lamballais et al. (1998); Maciel et al. (2003); Grundestam et al. (2008); Xia et al. (2016); Brethouwer (2017). Given the difficulty of performing experiments of this type, most of these studies are numerical, and most of them are conducted at low Reynolds number, $Re_\tau = u_\tau \delta/\nu \simeq 180 - 400$ (where u_τ is the friction velocity and δ the channel half-height). Recently, Brethouwer (2017) has performed a comprehensive set of calculations that reach $Re_\tau = 1505$, with Rotation numbers $Ro_b = 2\Omega\delta/U_b = 0 - 2.7$.

Among the findings of these investigations are: (1) the flow tends towards relaminarization on the cyclonic side at high Rotation numbers, while turbulence is amplified for moderate rotation rates; (2) elongated longitudinal vortices are formed; they may be responsible for strong (although infrequent) ejections that contribute to the Reynolds shear stress transport; (3) the mean velocity profile has a linear region with slope $2Ro_b$; in this layer the root-mean-square (rms) velocity fluctuations, the production of turbulent kinetic energy (TKE) and the dissipation are also linear; (4) the Reynolds stress anisotropy increases on the cyclonic side; and (5) oblique turbulent spots appear on the cyclonic side (Brethouwer, 2017).

While these studies have considered smooth walls, in most flows of engineering interest the surfaces are rough. The effect of roughness is opposite to that of cyclonic rotation: notably, the Reynolds shear stress is increased and the Reynolds stress anisotropy is decreased. It is important, to predict the flow in practical application, to understand how these opposite effects interact. Narasimhamurthy and Andersson (2015) considered ribbed channels subjected to spanwise rotation. The roughness was constituted by an array of square ribs, 40 wall units wide and high (the roughness height was one-tenth of the channel half-height), with a pitch equal to eight times the roughness height. The nominal Reynolds number was $Re_\tau = 400$. With this pitch, the flow can reattach between ribs; this type of rough surface is known as k-type (Perry and Joubert, 1969); in these conditions the flow is probably in the transitionally rough regime. They found that the effect of rotation and roughness are, indeed, opposite on the cyclonic side. As in studies of the smooth-wall case, they found that the modification of the Reynolds stresses was also indirect, mainly occurring through the change in the velocity gradient, but also due to the effect of the Coriolis production.

In the present study we perform a simulation of rotating channel flows over smooth and rough wall using sandgrain roughness. The simulations are designed to achieve the fully rough regime (at least on the anti-cyclonic side) while keeping the blockage very low. Compared to ribbed channels, sandgrain roughness is more representative of realistic surfaces encountered in many engineering applications, such as the blades of hydroelectric turbines.

In the following, the model will be formulated, and validated by comparison with the calculations of Hoyas and Jiménez (2006) and Brethouwer (2017). We will then discuss the results, and present some conclusions.

2. Problem formulation

The equations of conservation of mass and momentum for the incompressible flow of a Newtonian fluid are solved:

$$\frac{\partial u_i}{\partial x_i} = 0 \tag{1}$$

$$\frac{\partial u_i}{\partial t} + \frac{\partial}{\partial x_k}(u_k u_i) = -\frac{1}{\rho}\frac{\partial p}{\partial x_i} + \nu \nabla^2 u_i - 2\epsilon_{i3k}\Omega u_k + f_i - \delta_{i1}\frac{\Delta P}{\rho L}. \tag{2}$$

The indices 1, 2 and 3 represent the streamwise, wall-normal and spanwise directions (also denoted as x, y and z; the corresponding velocity components are u, v, and w). Ω is the channel rotation rate, oriented in the spanwise direction. The term f_i is used to enforce the no-slip boundary conditions inside the sandgrain roughness, modelled using an Immersed Boundary Method (IBM); $\Delta P/\rho L$ is the mean pressure gradient required to drive the flow. The equations of motion are solved using second-order accurate (in time and space) derivatives on a staggered mesh. The code is parallelized using MPI, and has been widely validated in a variety of turbulent flows over smooth and rough surfaces. Periodic boundary conditions are used in x and z, and no-slip conditions are used at the walls.

We use the virtual sand-paper model proposed by Scotti (2006). Each wall is subdivided into square tiles of size $2k$; in each tile, an ellipsoid with semiaxes k, $1.4k$ and $2k$ is placed, with its centre at $y = -0.5k$. Both the orientation and the placement in the (x, z)-plane of the ellipsoid are random. Periodicity of the elements is ensured at the streamwise and spanwise boundaries. The volume fraction of each grid cell occupied by the fluid, ϕ, is calculated in pre-processing, and at each step a force f_i is imposed after the corrector step to reduce the velocity in the cells occupied partially or fully by the roughness element. The roughness height, k, is 4% of the channel half-height, small enough to avoid blockage effects; with the model used, the roughness crest is $k_c = 1.5k$ (the longest axis of the ellipsoid is $2k$, and the wall is at $y = -0.5k$), and the mean roughness height is $\overline{k} = 0.6k$. Figure 1 shows a $\phi = 0.5$ isosurface, representative of the roughness shape, in a section of the channel. Details of the numerical

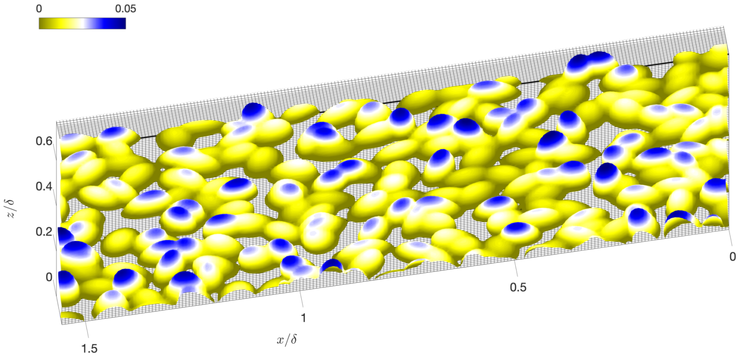

Figure 1: Volume of fluid, $\phi = 0.5$ isosurfaces, coloured by distance from the bottom wall. Every 8th grid line in y is shown.

implementation of the IBM can be found in the original paper or in Yuan and Piomelli (2014a).

We performed the direct numerical simulations at $Re_b = 19,000$ (based on channel height and bulk velocity); in the absence of rotation, this corresponds to $Re_\tau \simeq 960$ (based on channel half-height and friction velocity). Here, the wall stress τ_w is obtained by integrating the immersed-boundary force, f_1 in (2) (Yuan and Piomelli, 2014a). Wall stress and friction velocity averaged over both walls are denoted simply by τ_w and u_τ, while a subscript b or t refers to the bottom (anti-cyclonic, unstable) or top (cyclonic, stable) side. The average wall stress is defined as $\tau_w = (\tau_{w,b} + \tau_{w,t})/2$, and the friction velocity by $u_\tau^2 = \tau_w$. The calculations were performed in a domain with dimensions 12δ and 6δ in the streamwise and spanwise directions; in the normal direction the domain size was 2δ when the wall was smooth, and 2.064δ in the rough-wall case to account for the blockage due to the roughness (the zero-plane displacement at each side by the roughness is $d = 0.8k = 0.032\delta$). $1536\times192\times768$ grid points were used for the smooth cases, and $1536\times530\times768$ for the rough ones. The mass-flow rate was kept constant, so that $Re_b = 19,000$ for all cases but Re_τ varied between 960 and 490 for the smooth-wall cases, and between 1,500 and 780 for the rough-wall ones. Three rotation rates were examined: $Ro_b = 2\Omega\delta/U_b = 0$, 0.42 and 1.0, and $Ro_\tau = 2\Omega\delta/u_\tau$ between 0 and 39. Table 1 summarizes the simulation parameters.

3. Results and discussion

3.1. Model validation

The roughness model itself has been extensively validated in the transitional and fully rough regimes (Scotti, 2006; Yuan and Piomelli, 2014b, 2015; Wu and Piomelli, 2018). We also compared our results with the simulation by Hoyas and Jiménez (2006) (referred to as HJ06) for the non-rotating case, and with that of Brethouwer (2017) (referred to as B17) for the case with intermediate

Case	Walls	Ro_b	Ro_τ	Re_τ	$Re_{\tau,b}$	$Re_{\tau,t}$
S00	Smooth	0.00	0	960	960	960
R00	Rough	0.00	0	1,500	1,500	1,500
S04	Smooth	0.42	10	810	960	610
R04	Rough	0.42	6	1,380	1,640	1,070
S10	Smooth	1.00	39	490	600	340
R10	Rough	1.00	24	780	950	560
HJ06	Smooth	0.00	0	933	933	933
B17	Smooth	0.45	11.2	800	964	594

Table 1: Summary of simulation parameters. HJ06 and B17 refer, respectively, to the simulation data of Hoyas and Jiménez (2006) and Brethouwer (2017).

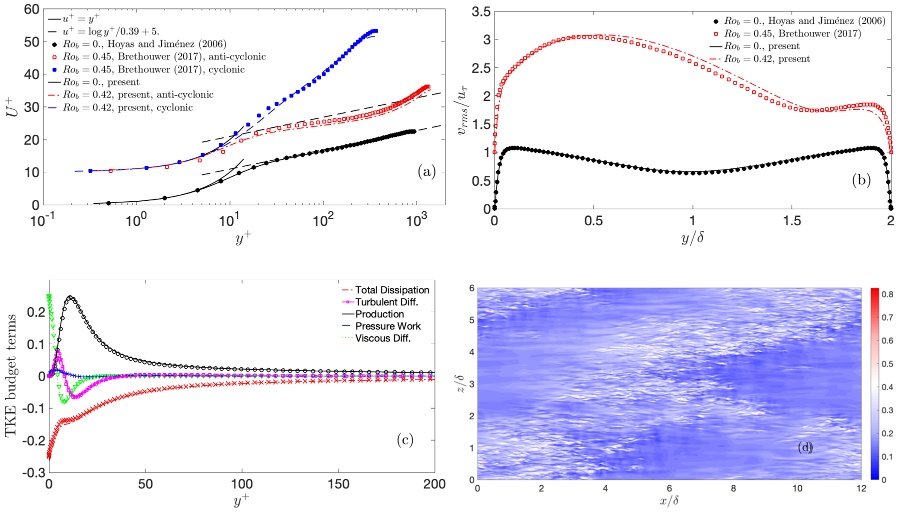

Figure 2: (a) Mean velocity profiles in inner units (the two sets of curves are shifted by 5 units). (b) Wall-normal root-mean-square velocity fluctuation (the two sets of curves are shifted by one unit). (c) Turbulent kinetic energy budgets at $Ro_b = 0$; lines: present simulation; symbols: Hoyas and Jiménez (2006). (d) Contours of instantaneous streamwise velocity u in the plane $y_w = 0.01$ on the cyclonic (stable) side at $Ro = 0.42$.

rotation (B17 uses $Re_b = 20,000$ and $Ro_b = 0.45$ so some slight difference can be expected). For the S00 case, the present grid spacing in wall units is $\Delta x^+ = \Delta z^+ = 7.4$. HJ06 use 7.6 and 3.8, respectively, and a spectral method; their domain is also approximately twice as long in both directions. For the R04 case, the grid size is $\Delta x^+ = \Delta z^+ = 6.2$. For the corresponding case, B17 uses a domain of the same size as HJ06, and $\Delta x^+ = 9.8$, $\Delta z^+ = 4.9$. The wall-normal grid is finer in both reference calculations; even using a smaller number of points, however, the first grid point is at $y^+ = 0.36$, and we have 11 points below $y^+ = 10$.

The present results, shown in Figure 2, compare well with the reference data. For the case $Ro_b = 0$ the agreement is excellent both for the mean velocity (normalized here by the local friction velocity, $u_{\tau,b}$ or $u_{\tau,t}$), for the wall-normal velocity fluctuation v_{rms} (normalized by the average u_τ) and for the terms in the turbulent kinetic energy budget. For the rotating case, the agreement on velocity and v_{rms} is also quite good, considering the difference in rotation rates. The instantaneous flow visualization, shown in Figure 2(d), also presents the same features observed by Brethouwer (2017) (in particular, note the oblique band-like structures that compare well with those shown in Figure 1*(e)* in the paper cited).

3.2. Double averaging

It is usual, for a plane channel flow, to decompose a variable into a mean component obtained by averaging in time and in the (x, z)-plane, and a deviation from the mean. In rough-wall boundary layers, first we define the time averaging operator, indicated by an overbar; then, we can define two types of spatial averaging (Nikora et al., 2007). The *intrinsic* spatial average (denoted by $\langle\cdot\rangle$) is carried out in the (x, z)-plane, in the fluid domain only, while the *superficial* average $\langle\cdot\rangle_s$ is carried out over the whole plane. Then, an alternative decomposition can be used (Raupach et al., 1991; Nikora et al., 2007; Mignot et al., 2009), in which a quantity is split into a time-averaged part and a fluctuation (denoted by a prime); the time-averaged part, in turn, can be separated into a time- and space-averaged (or *double-averaged*) component, and the spatial variation of the time average, denoted by a tilde:

$$\theta(x,y,z,t) = \overline{\theta}(x,y,z) + \theta'(x,y,z,t) = \left\langle\overline{\theta}\right\rangle(y) + \widetilde{\theta}(x,y,z) + \theta'(x,y,z,t). \quad (3)$$

The spatial variation of the time average $\widetilde{\theta}$ is also known as the "wake field", or "form-induced perturbation". The wake perturbations —such as $\partial\widetilde{u}_i/\partial x_j$ and $\widetilde{u_i'u_j'}$— have been shown to play an important role in the destabilization of the flow and in the redistribution of energy between the normal Reynolds stresses (Yuan and Piomelli, 2014b). Note that in smooth cases and above the crest the superficial and intrinsic average are identical, and a double-averaging is identical to the usual space- and time-averaging.

3.3. Mean velocity

Figure 3 shows the mean velocity profiles, in outer and inner units, for the six calculations. $d = 0.8k$ is the virtual origin, chosen as the line of application

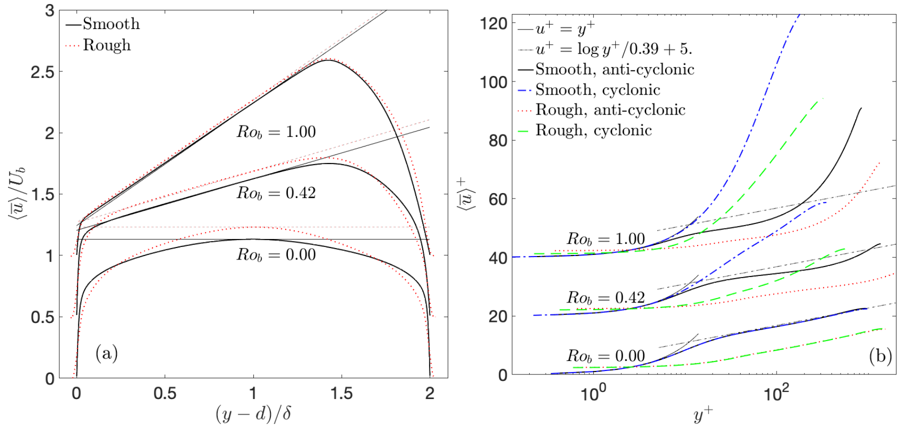

Figure 3: Double-averaged velocity profiles in (a) outer units and (b) wall units (defined using $u_{\tau,b}$ and $u_{\tau,t}$, and, in the rough-wall case, $y-d$). The profiles are shifted by 0.5 units in (a) and 20 units in (b) for clarity.

of the force on the roughness elements (Jackson, 1981; Scotti, 2006). In outer units, we observe that the linear region with slope 2Ω is present. This is a region of neutral stability that separates the stable and unstable sides (Johnston et al., 1972), where the mean vorticity $2\Omega - d\langle \overline{u} \rangle / dy$ is zero. Its extent is known to depend on the Reynolds number, as well as on the rotation rate (Johnston et al., 1972; Grundestam et al., 2008). When the wall is rough the neutrally stable region begins further away from the wall, compared to the smooth-wall case, especially for the intermediate rotation rate. In inner variables, a logarithmic region is observed on the unstable side, whose extent decreases with Ro_b. On the stable side no logarithmic layer is observed when rotation is applied, either in the rough-wall or in the smooth-wall cases.

Figure 4 shows the difference between the velocity in the smooth and rough cases (subscripts s and r, respectively) in wall units, $\langle \overline{u} \rangle_s^+ - \langle \overline{u} \rangle_r^+$, on the unstable side. The quasi-constant region corresponds to the shift in the log law, the roughness function ΔU^+, which was calculated as the average of $\langle \overline{u} \rangle_s^+ - \langle \overline{u} \rangle_r^+$ over the nearly constant region, and is shown in Figure 4 (a). The roughness function can be related to the equivalent sandgrain roughness k_s (the height of the sand-grain roughness that gives the same drag as the surface in question). We use here the relation proposed by Colebrook (1939)

$$\Delta U^+ = \frac{1}{\kappa} \log\left(1 + 0.26 k_s^+\right) \tag{4}$$

to obtain $k_s^+ = 94$, 57 and 21 for the cases R00, R04 and R10, respectively (Figure 4(b)). The ratio k_s^+/k^+ is 1.6, 0.87 and 0.56. Previous calculations with this roughness model give $k_s^+/k^+ \simeq 1.6$ in the fully rough regime, and $k_s^+/k^+ \simeq 1$ when the roughness is transitional (Figure 4(c)). The fact that, in the rotating case, these ratios have much lower values than in the non-rotating

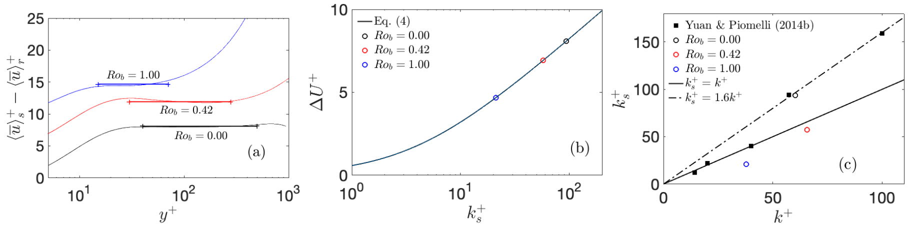

Figure 4: (a) Velocity difference between smooth and rough-wall cases (each profile is shifted by 5 units for clarity); the thick line indicates the roughness function, and the region over which the averaging is performed. (b) Equivalent sandgrain roughness height. (c) k_s^+ *vs.* k^+.

one suggests that some fundamental changes to the effect of roughness are caused by the rotation. The value of k_s is regularly used in turbulence models used in industrial applications; thus, the different relationship between the geometric roughness height and its effect on the friction, as measured by k_s, may be an important issue for these applications.

The Reynolds stresses $\left\langle\overline{u_i'u_j'}\right\rangle$ are shown in Figure 5, normalized using the average τ_w. In $Ro_b = 0.42$ case, their behaviour is consistent with the results of Narasimhamurthy and Andersson (2015) for $Ro_\tau = 6$, despite the fact that they considered a very different type of roughness. On the cyclonic side, the stabilizing effect of the rotation is counterbalanced by the destabilization caused by the roughness, and a clear difference is observed between rough- and smooth-wall cases. On the unstable side, on the other hand, roughness has a lesser effect, and Townsend's similarity hypothesis (the rms fluctuations are independent of roughness, when scaled with the friction velocity) applies to the u' fluctuations, although not to v' and w'. A remarkable difference can be observed at the highest rotation rate: with a smooth wall, $\left\langle\overline{u'v'}\right\rangle$ is negligible on the stable side, where the flow anisotropy increases as $\left\langle\overline{u'u'}\right\rangle$ decreases less than $\left\langle\overline{v'v'}\right\rangle$. When the wall is rough, on the other hand, the flow is more disturbed (as will be shown momentarily), resulting in a more turbulent-like profile. Note that the total shear stress is indeed linear if the dispersive and viscous stresses are included. The dispersive stresses are non-zero in the channel interior, perhaps due to large-scale motions that have been observed by several researchers, in flows over smooth and rough surfaces (**???**).

The dispersive stresses $\langle\widetilde{u}_i\widetilde{u}_j\rangle$ in the roughness layer and immediately above it are shown in Figure 6. On both sides, they are comparable to the Reynolds stresses. Moderate rotation does not affect either the Reynolds or the dispersive stresses very much, at least not in their qualitative behaviour. On the unstable side both $\left\langle\overline{u'u'}\right\rangle$ and $\langle\widetilde{u}\widetilde{u}\rangle$ decrease with rotation number; their ratio does not change significantly, however. The 22 and 12 components of either Reynolds or dispersive stresses are not affected at all, while $\left\langle\overline{w'w'}\right\rangle$ increases. On the stable side, moderate rotation causes very slight decreases of both Reynolds and dispersive stresses.

At the highest rotation rate, more significant changes are observed: on the

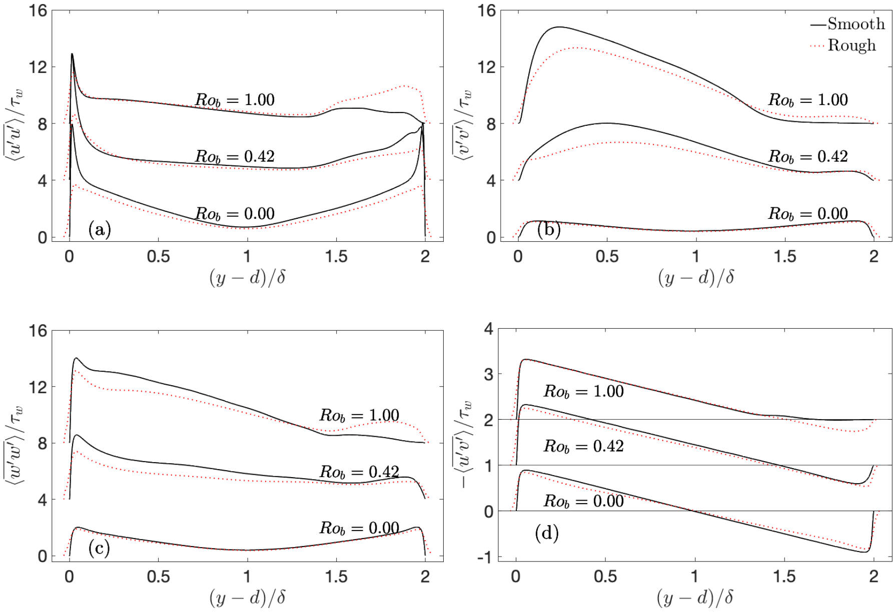

Figure 5: Double-averaged Reynolds stress profiles. (a) $\left\langle\overline{u'u'}\right\rangle$; (b) $\left\langle\overline{v'v'}\right\rangle$; (c) $\left\langle\overline{w'w'}\right\rangle$; (d) $-\left\langle\overline{u'v'}\right\rangle$. The Reynolds stresses are normalized by the average τ_w. The profiles are shifted by 4 units in (a-c) and one unit in (d), for clarity.

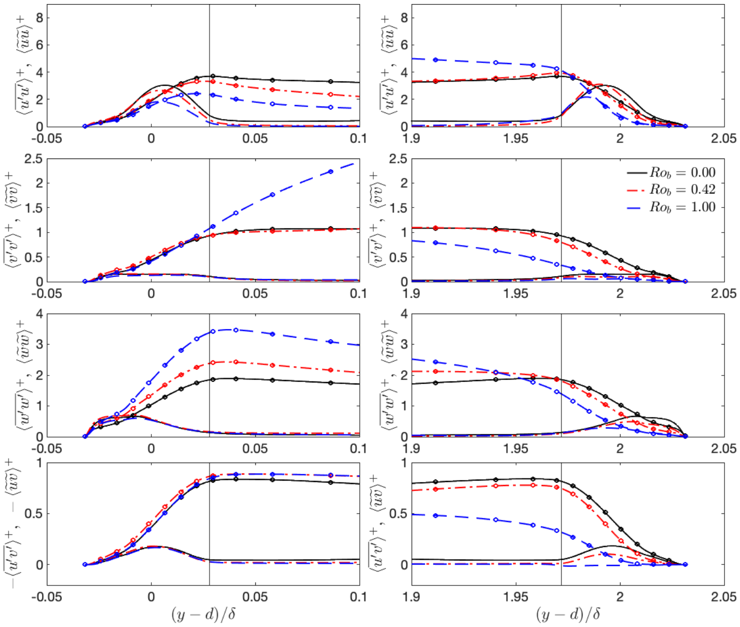

Figure 6: Dispersive stresses and Reynolds stresses. Lines: Dispersive stresses $\langle \widetilde{u}_i \widetilde{u}_j \rangle$; Lines with symbols: Reynolds stresses $\langle \overline{u_i' u_j'} \rangle$. The thin solid line represents the position of roughness crest.

unstable side $\left\langle \overline{v'v'} \right\rangle$ and $\left\langle \overline{w'w'} \right\rangle$ increase significantly (but their respective dispersive components do not). On the stable side $\left\langle \overline{v'v'} \right\rangle$, $\left\langle \overline{u'v'} \right\rangle$ and $\left\langle \overline{w'w'} \right\rangle$ all decrease inside the roughness sublayer; this may be due to the fact that the flow develops towards the transitionally rough regime. The roughness sublayer thickness—defined as the near-wall region where the form-induced perturbation is strong—appears insensitive to Ro_b. The linear region of the mean velocity (Figure 3(a)), however, begins further from the wall in the cases with roughness; this, and the fact that Townsend's similarity holds only partially, indicates that rotation tends to propagate the effects of roughness away from the wall. The advection caused by the longitudinal vortices that are formed in rotating flows may be at least partly responsible for this effect. The decrease of $\langle \widetilde{u}_i \widetilde{u}_j \rangle^+$ with increasing Ro_b on the stable side is probably due to the flow entering the transitionally rough regime. A similar increase of $\langle \widetilde{u}_i \widetilde{u}_j \rangle^+$ for non-rotating flow going from the transitional to the fully rough regime was was also observed by Yuan and Piomelli (2014b, 2015).

The Reynolds stress anisotropy tensor is defined as

$$b_{ij} = \frac{\left\langle \overline{u_i' u_j'} \right\rangle}{\left\langle \overline{u_k' u_k'} \right\rangle / 2} - \frac{2}{3}\delta_{ij}; \tag{5}$$

b_{11} and b_{22} are shown in Figure 7. Both rotation and roughness affect the

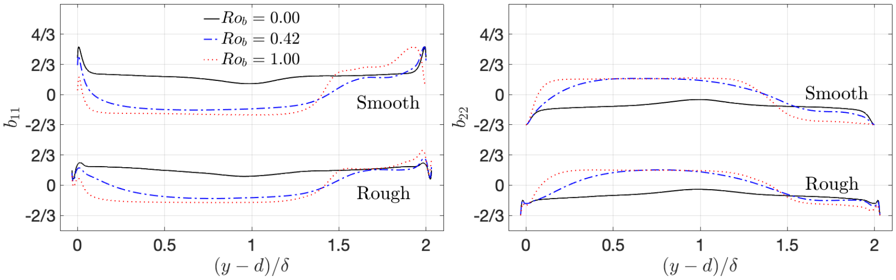

(a) (b)

Figure 7: Reynolds stress anisotropy tensor. (a) 11 component; (b) 22 component.

anisotropy of the Reynolds stresses. The effect of roughness is, as expected, restricted to the roughness sublayer, and tends to decrease the flow anisotropy.

These effects can be better understood if one considers Lumley's invariant map (Lumley, 1978; Pope, 2000; Durbin and Pettersson Reif, 2011), shown in Figure 8. In this map the invariants of the stress anisotropy tensor are considered. They are defined as

$$\mathrm{II}_b = -b_{ij}b_{ji}/2; \qquad \mathrm{III}_b = b_{ij}b_{jk}b_{ki}/2. \tag{6}$$

All possible turbulence states must lie within this triangle. It is bounded by lines corresponding, on the right, to axisymmetric expansion, on the left, to axisymmetric compression, and, on the upper side, to two-component turbulence. The three vertices correspond to isotropic turbulence (bottom), one-component turbulence (top right) and two-component, axisymmetric turbulence (upper left).

In the non-rotating case, when the wall is smooth, turbulence is in the two-component state near the wall, shifting to an axisymmetric expansion in the logarithmic layer and tending towards isotropic turbulence at the channel centre. When the wall is rough, the Reynolds stress anisotropy is much decreased in the near-wall region, as is well known from experimental results (Flack et al., 2007). In the roughness sublayer, turbulence is near the axisymmetric compression line, instead of the axisymmetric expansion. This may be due (Busse and Sandham, 2012) to the fact that the streamwise stresses are damped in this region: close to the wall the ratios between the normal components are $\langle \overline{u'u'} \rangle : \langle \overline{w'w'} \rangle : \langle \overline{v'v'} \rangle = 3 : 3 : 1$, as opposed to $8 : 2 : 1$ in the smooth channel. Thus, $\mathrm{III} \leq 0$, and the Reynolds stress tensor becomes an oblate spheroid, rather than a prolate one.

On the stable side, for the smooth wall, the two-component state extends much farther away from the wall when rotation is applied. This is due to the increased flow organization brought about by the rotation, which causes the vortical structures to align with the $x-$axis (Lamballais et al., 1998); this behaviour is associated with the large longitudinal vortices. Roughness tends to reduce this phenomenon: the trend towards the axisymmetric expansion and the two-component limit is weaker, although more pronounced at the edge of the roughness sublayer.

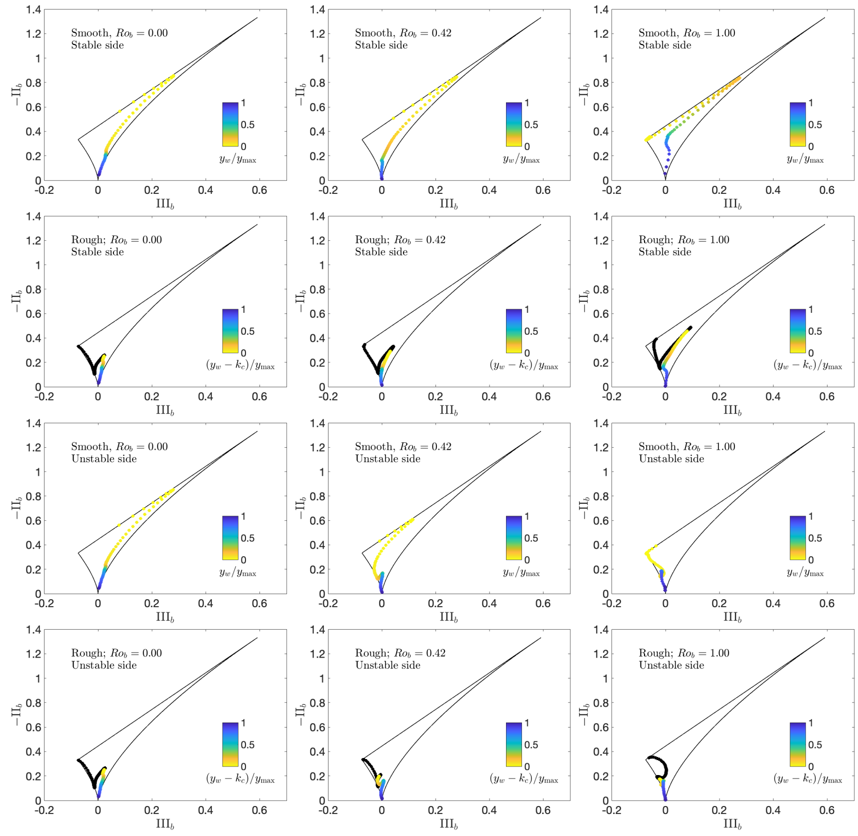

Figure 8: Anisotropy map of the Reynolds stresses. The columns correspond (from left to right) to $Ro_b = 0$, 0.42 and 1.00. First and third rows are for the smooth wall, stable and unstable side, respectively. Second and fourth row are for the rough wall, stable and unstable side. y_w is the distance to the nearest wall and $y_{\max}$ is the location of maximum velocity. Black dots indicate locations below the roughness crest.

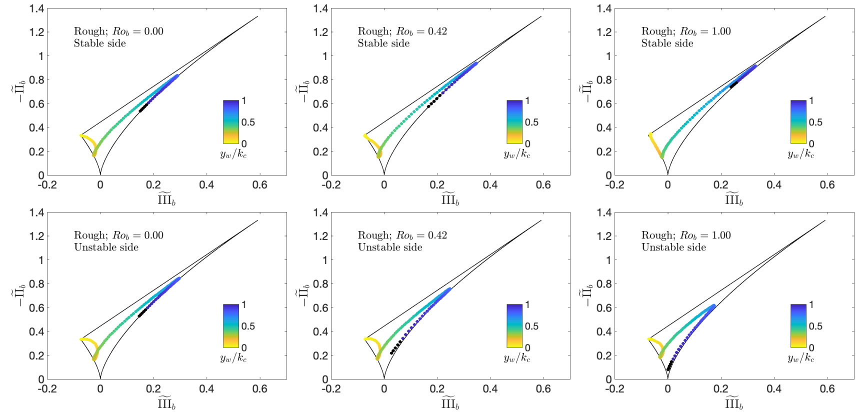

Figure 9: Anisotropy map of the dispersive stresses. The columns correspond (from left to right) to $Ro_b = 0$, 0.42 and 1.00. First row is for the stable side, second row for the unstable one. y_w is the distance to the nearest wall.

On the unstable side, when rotation is applied, turbulence tends to depart from the two-component state, as the v and w fluctuations increase relative to u (Figure 5); at the highest rotation rate the entire layer is close to the axisymmetric compression limit. Roughness enhances this effect. This behaviour is analogous to that observed when $Ro_b = 0.00$.

Anisotropy invariants can be calculated for the dispersive stresses as well (Figure 9). They are denoted as $\widetilde{\mathrm{II}}_b$ and $\widetilde{\mathrm{III}}_b$. The state of the dispersive stresses is much closer to the two-component and axisymmetric expansion lines. This behaviour is due to the fact that, in the roughness sublayer, the flow is preferentially moving in channels between roughness elements. This phenomenon is illustrated in Figure **??**, which shows contours of the wake velocity for the $Ro_b = 0$ and 1.00 cases. In addition to the channels, characterized by large $\widetilde{u}$, and $\widetilde{w} > \widetilde{v}$, we observe "dead-water" zones immediately behind the roughness elements. These effects persist when rotation is present, although the magnitude of the wake components is reduced.

The joint probability-density functions (JPDFs) of the wake velocity components (Figure 11) confirm these observations: large values of $\widetilde{u} > 0$ are preferentially associated with large $\widetilde{w}$ (the JPDF of $[\widetilde{u}, \widetilde{w}]$ has a very narrow peak near $\widetilde{v} = 0$) because the fluid tends to travel around, rather than over, the roughness elements. When $\widetilde{u} < 0$, on the other hand, the $[\widetilde{u}, \widetilde{w}]$ JPDF shrinks, forming a peak associated with small values of $\widetilde{w}$ and $vtil$, representing the dead-water zones. Therefore, in the anisotropy map, the dispersive stress is much closer to the 2D axisymmetric expansion lines (i.e., right boundary of the Lumley triangle, rod-like turbulence with one large eigenvalue) at this wall-normal distance. When rotation is present, on the unstable side the magnitude of $\widetilde{u}$ decreases and the $\widetilde{u} > 0$ events dominate the $\widetilde{u}, \widetilde{w}$ JPDF. $\widetilde{u}$ and $\widetilde{w}$ are comparable in the channels and $\widetilde{v}$ remains small. The dead-water zones become less prominent

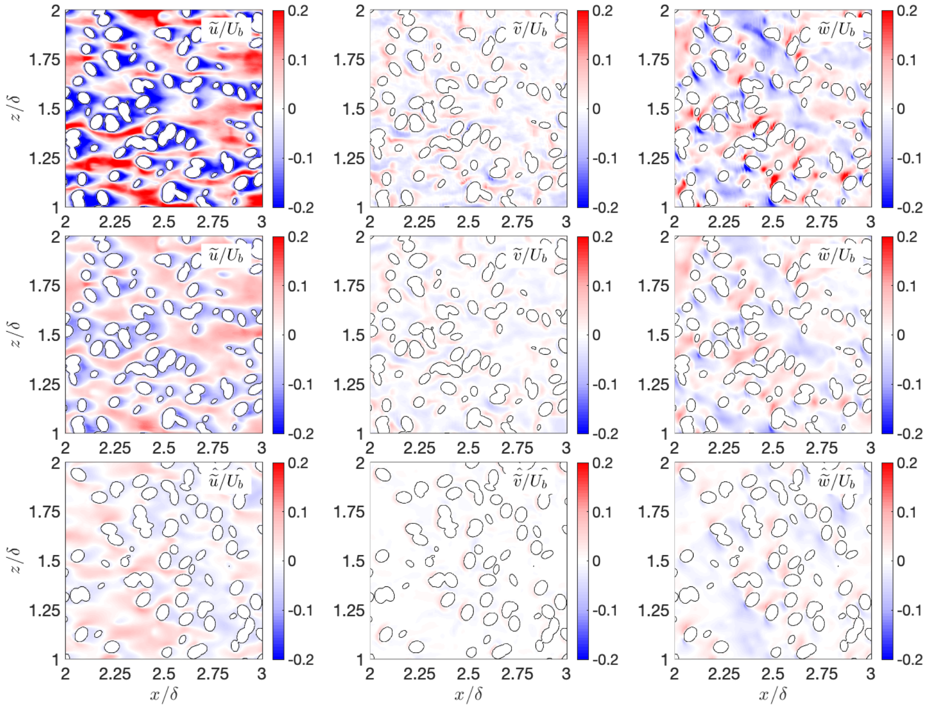

Figure 10: Contours of wake-velocity components at $y_w d = d = 0.53k_c$. Top row: $Ro_b = 0$; middle row: $Ro_b = 1.0$, unstable side; bottom row: $Ro_b = 1.0$, stable side.

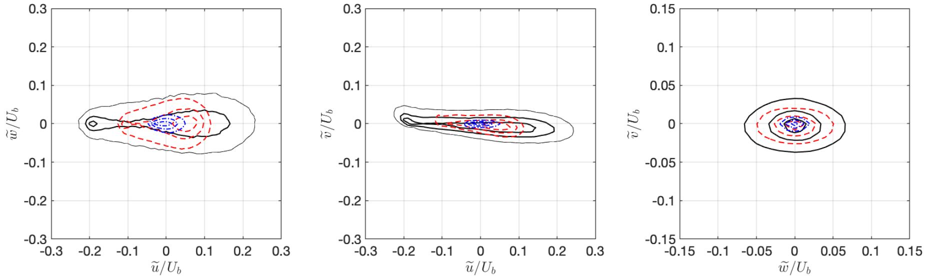

Figure 11: Joint-PDF of wake components at $y_w = d = 0.53k_c$. Each JPDF is normalized by its maximum value and plotted at levels $[0.8, 0.5, 0.2]$. The locations where VOF is less than 1 are excluded. Bin size is $0.01U_o$ and $0.25U_o/\delta_o$. ——— , $Ro_b = 0$; - - - , $Ro_b = 1.0$ unstable side; —·—· , $Ro_b = 1.0$ stable side.

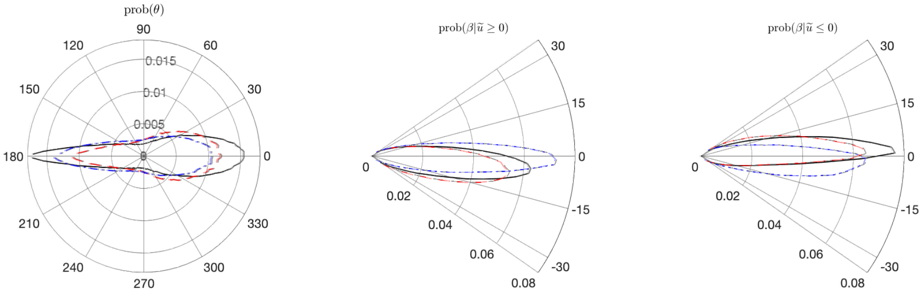

Figure 12: Probability of flow direction of the wake field. For β, on the left side the probability is conditionally sampled with $\widetilde{u} \geq 0$, and on the right with $\widetilde{u} < 0$. Bin size is 0.01π. ——— $Ro_b = 0$; - - - $Ro_b = 1.0$ unstable side; -·- $Ro_b = 1.0$ stable side.

than in the non-rotating case. This may cause the anisotropy of the dispersive stress to move away from the one-component limit on the unstable side, due to the destabilization effect of rotation. The wake flow is still highly parallel to the $x - z$ plane, with slightly more transverse motion when $\widetilde{u} > 0$. On the stable side, all the three components are small compared to the ones on the unstable side. The wake flow is still highly 2D ($\widetilde{v} \sim 0$).

We can also examine the flow angle in the $x - z$ plane, $\theta = \mathrm{atan2}(\widetilde{w}, \widetilde{u})$ (the four-quadrant inverse tangent, $\theta \in [-\pi, \pi]$), and in the vertical direction, $\beta = \mathrm{atan2}(\widetilde{v}, \sqrt{\widetilde{u}^2 + \widetilde{w}^2}) \in [-\pi/2, \pi/2]$ ($\theta = 0$ is the positive-x direction, and $\beta = 0$ is the horizontal direction). They are shown in Figure 12. The flow in the $x - z$ plane rarely deviates from the x-direction, especially in the recirculation region. The probability of β clearly shows that the wall-normal motion is weak, especially when $\widetilde{u} < 0$. When $\widetilde{u} \geq 0$ there is a slight preference for sweeping events, which is reasonable because the mini-channel flow may be more likely to occur when the local roughness height decreases in the direction of the flow and forms a basin, generating a downwash.

The same analysis can be carried out deeper in the sublayer (not shown). Here recirculation regions downstream of roughness elements dominate the wake. The positive streamwise velocity due to channeling becomes much weaker, $\widetilde{w}$ is comparable to $\widetilde{u}$, and $\widetilde{v}$ decreases significantly, compared to the wake at $y_w = 0.53k_c$. The anisotropy of the dispersive stress, therefore, approaches the 2D-axisymmetric contraction (i.e., two large eigenvalues). The wake flow is still highly parallel to the $x - z$ plane, and the transverse flow is more significant than further away from the wall.

3.4. Reynolds-stress budgets

The budget of the time- and superficially averaged Reynolds stresses $\left\langle \overline{u_i'u_j'} \right\rangle_s$, in a rotating channel flow, can be written as

$$0 = \mathcal{T}_{ij} + \nu\nabla^2 \left\langle \overline{u_i'u_j'} \right\rangle_s + \mathcal{P}_{ij} + \Pi_{ij} - \varepsilon_{ij} + \mathcal{R}_{ij}. \tag{7}$$

The terms on the right-hand-side of (7) are, respectively, the turbulent transport, viscous diffusion, production, pressure work (or velocity-pressure-gradient), the dissipation, and and the rotation term. They are defined as

$$\mathcal{T}_{ij} = -\frac{\partial}{\partial x_k}\left\langle \overline{u'_i u'_j u'_k} + \widetilde{u}_i \widetilde{u}_j \widetilde{u}_k \right\rangle_s \tag{8}$$

$$\Pi_{ij} = -\frac{1}{\rho}\left[\left\langle \overline{u'_i \frac{\partial p'}{\partial x_j}} \right\rangle_s + \left\langle \overline{u'_j \frac{\partial p'}{\partial x_i}} \right\rangle_s\right] \tag{9}$$

$$\varepsilon_{ij} = 2\nu \left\langle \overline{\frac{\partial u'_j}{\partial x_i}\frac{\partial u'_i}{\partial x_j}} \right\rangle_s \tag{10}$$

$$\mathcal{R}_{ij} = -2\Omega\left[\epsilon_{i3k}\left\langle \overline{u'_j u'_k}\right\rangle_s + \epsilon_{j3k}\left\langle \overline{u'_i u'_k}\right\rangle_s\right] \tag{11}$$

The pressure-velocity-gradient correlation can be split into pressure-diffusion and pressure-strain terms:

$$\Pi_{ij} = -\frac{1}{\rho}\left[\frac{\partial \left\langle \overline{u'_i p'}\right\rangle_s}{\partial x_j} + \frac{\partial \left\langle \overline{u'_j p'}\right\rangle_s}{\partial x_i}\right] + \frac{1}{\rho}\left\langle \overline{p'\left(\frac{\partial u'_i}{\partial x_j} + \frac{\partial u'_j}{\partial x_i}\right)} \right\rangle_s = \Pi^d_{ij} + \Pi^s_{ij} \tag{12}$$

Because of the double-averaging, the production term can be written as (Raupach et al., 1991; Nikora et al., 2007; Mignot et al., 2009):

$$\begin{aligned}
\mathcal{P}_{ij} =& -\left(\left\langle \overline{u'_i u'_k}\frac{\partial \overline{u_j}}{\partial x_k}\right\rangle_s + \left\langle \overline{u'_j u'_k}\frac{\partial \overline{u_i}}{\partial x_k}\right\rangle_s\right) \\
=& -\left(\left\langle \overline{u'_i u'_k}\right\rangle_s \frac{\partial \left\langle \overline{u_j}\right\rangle}{\partial x_k} + \left\langle \overline{u'_j u'_k}\right\rangle_s \frac{\partial \left\langle \overline{u_i}\right\rangle}{\partial x_k}\right) \\
& -\left(\left\langle \overline{u'_i u'_k}\right\rangle_s \left\langle \frac{\partial \widetilde{u}_j}{\partial x_k}\right\rangle + \left\langle \overline{u'_j u'_k}\right\rangle_s \left\langle \frac{\partial \widetilde{u}_i}{\partial x_k}\right\rangle\right) \\
& -\left(\left\langle \widetilde{u'_i u'_k}\frac{\partial \widetilde{u}_j}{\partial x_k}\right\rangle_s + \left\langle \widetilde{u'_j u'_k}\frac{\partial \widetilde{u}_i}{\partial x_k}\right\rangle_s\right) && (13) \\
=& \mathcal{P}^s_{ij} + \mathcal{P}^m_{ij} + \mathcal{P}^w_{ij} && (14)
\end{aligned}$$

The first term on the RHS of (14) is the “shear production”, while the other two are due to the wake fluctuations (the last one is known as “wake production”). Their sum, $\mathcal{P}^{fi}_{ij} = \mathcal{P}^w_{ij} + \mathcal{P}^m_{ij}$, is the contribution of the form-induced perturbations to the Reynolds-stress production.

The additional term $\mathcal{R}_{ij}$ is due to the work of the Coriolis force. On the unstable side of the channel, where the Reynolds shear stress is negative, this term tends to transfer energy from the streamwise to the wall-normal fluctuations, whereas on the stable side the opposite occurs. The contribution of this term to the 11 and 22 stresses is equal and opposite, so that the TKE is only affected by rotation indirectly, through the modifications to the shear stresses and mean velocity profiles. It may be combined with the shear production to yield a total production term (Brethouwer, 2017), $\mathcal{P}^{tot}_{ij} = \mathcal{P}^s_{ij} + \mathcal{R}_{ij}$.

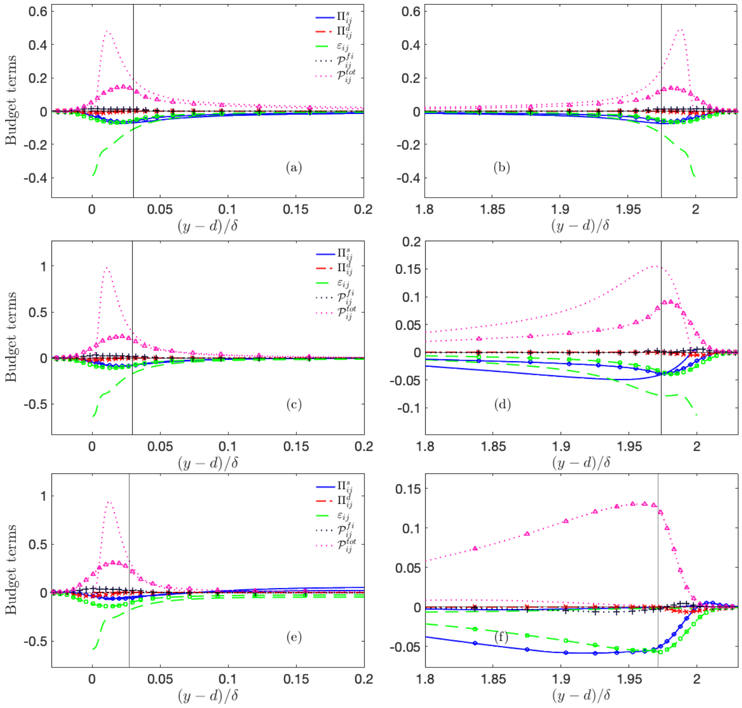

Figure 13: Selected terms in the budget of $\left\langle \overline{u'u'} \right\rangle$, normalized by $u_{\tau,avg}$ and ν. (a,b) $Ro_b = 0.00$; (c,d) $Ro_b = 0.42$; (e,f) $Ro_b = 1.00$. Lines: smooth wall; lines with symbols: rough wall. The black line indicates the location of the roughness crest.

Selected terms of the Reynolds-stress budgets are shown in Figures 13-15. On the unstable side, the shear production of $\langle\overline{u'u'}\rangle$ is significant only very near the wall, peaking around $(y-d)^+ \simeq 12$, as expected (Figure 13). Roughness decreases the peak production, as also observed by Yuan and Piomelli (2014b). On the stable side, on smooth walls, rotation decreases the magnitude of all terms; on the rough wall both the magnitude of all terms and u_τ increase. At $Ro_b = 0.42$ these effects roughly balance each other, but at $Ro_b = 1.00$ the fact that significant fluctuations (and Reynolds stresses) are present in the rough-wall case (and not in the smooth one) results in much larger values of total production (mostly due to the shear component), balanced by the pressure work and viscous dissipation, which are comparable in magnitude.

Moving to the budget of $\langle\overline{v'v'}\rangle$, Figure 14, we observe that when the wall is smooth the rotation term acts as a source on the unstable side (since $\mathcal{P}^s_{22} = 0$, $\mathcal{P}^{tot}_{22} = \mathcal{R}_{22}$). When the wall is rough, the form-induced production plays a role, which, however, decreases with the rotation rate. When the wall is smooth the pressure-strain removes energy from the v' fluctuations when the channel is rotating (a behaviour opposite to non-rotating case), redistributing it to $\langle\overline{u'u'}\rangle$ and $\langle\overline{w'w'}\rangle$ stresses, as discussed by Brethouwer (2017). The pressure-diffusion, however, is not negligible, and has the opposite sign; the combined effect of pressure diffusion and pressure-strain correlations is always to increase $\langle\overline{w'w'}\rangle$ and decrease $\langle\overline{u'u'}\rangle$; for $Ro_b = 0$ and 0.42 the pressure work has a positive contribution to $\langle\overline{v'v'}\rangle$, while for the highest rotation rate it is removing energy from it. When the wall is rough Π^d_{22} is negligible, and the pressure-strain correlation redistributes energy from $\langle\overline{u'u'}\rangle$ to $\langle\overline{v'v'}\rangle$ and $\langle\overline{w'w'}\rangle$ for $Ro_b = 0$ and 0.42, and from $\langle\overline{v'v'}\rangle$ to $\langle\overline{u'u'}\rangle$ and $\langle\overline{w'w'}\rangle$ for the highest rotation rate (except near the roughness crest, where Π^s_{11} and Π^d_{11} are negative). This phenomenon was also observed by Narasimhamurthy and Andersson (2015).

On the stable side, rotation redistributes energy from $\langle\overline{v'v'}\rangle$ to $\langle\overline{u'u'}\rangle$, while the pressure-strain correlation redistributes it from $\langle\overline{v'v'}\rangle$ to $\langle\overline{u'u'}\rangle$ and $\langle\overline{w'w'}\rangle$. The rotation term (and hence the total production) is much larger when the wall is rough, due to the increased shear stress $\langle\overline{u'v'}\rangle$. The form-induced production is also significant, except at the highest rotation rate.

The budget for the Reynolds shear stress, $\langle\overline{u'v'}\rangle$, is shown in Figure 15. On the unstable side, the total production increases the magnitude of $\langle\overline{u'v'}\rangle$. Pressure diffusion is negligible away from the wall ($y^+ > 30$) when the wall is smooth; it is always small when roughness is present. The pressure-strain correlation is always positive, as is the sum of pressure strain and pressure diffusion (i.e., the pressure work decreases the magnitude of the shear stress). When roughness is present the form-induced production is significant, nearly equal to the shear production P^s_{12}.

On the stable side, at the highest rotation rate the total production becomes negative (i.e., decreases the magnitude of $\langle\overline{u'v'}\rangle$) when the wall is smooth (although the shear production is positive). Roughness results in significant form-induced production, as well as increased shear production. These production terms result in more significant $\langle\overline{u'v'}\rangle$ levels than observed in the smooth-wall

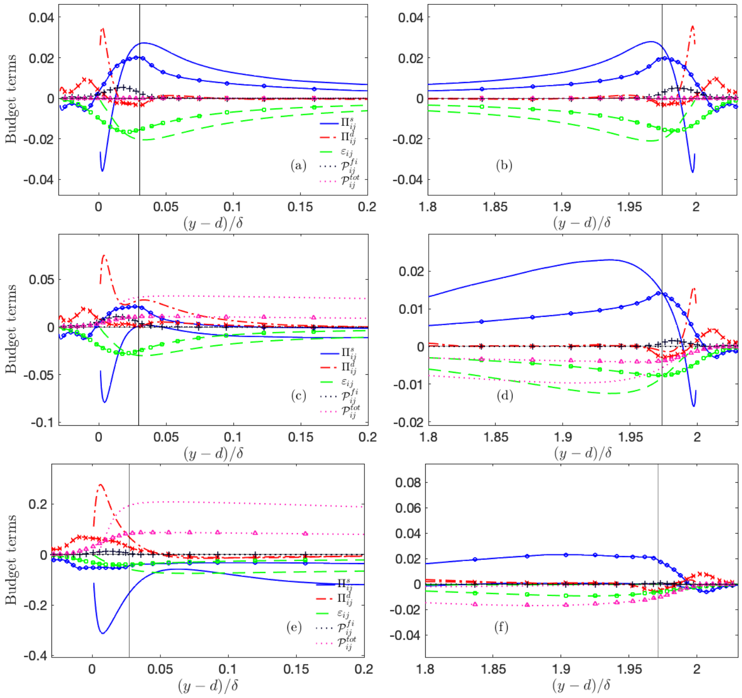

Figure 14: Selected terms in the budget of $\left\langle \overline{v'v'} \right\rangle$, normalized by $u_{\tau,avg}$ and ν. (a,b) $Ro_b = 0.00$; (c,d) $Ro_b = 0.42$; (e,f) $Ro_b = 1.00$. Lines: smooth wall; lines with symbols: rough wall. The black line indicates the location of the roughness crest.

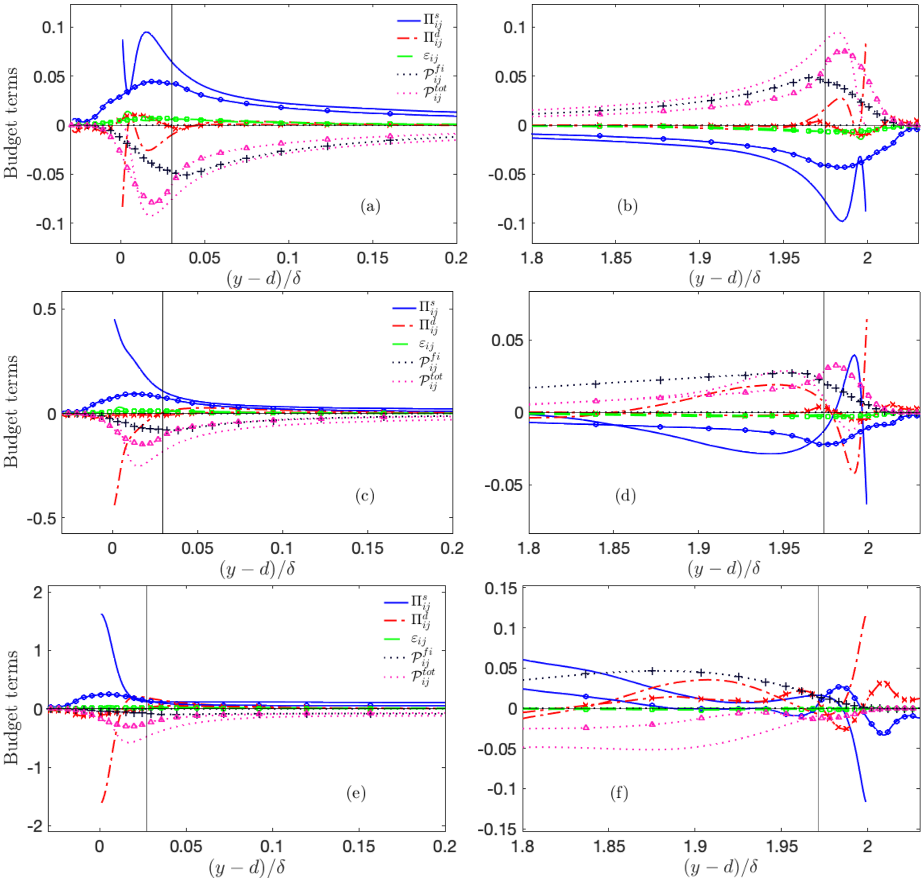

Figure 15: Selected terms in the budget of $\left\langle \overline{u'v'} \right\rangle$, normalized by $u_{\tau,avg}$ and ν. (a,b) $Ro_b = 0.00$; (c,d) $Ro_b = 0.42$; (e,f) $Ro_b = 1.00$. Lines: smooth wall; lines with symbols: rough wall. The black line indicates the location of the roughness crest.

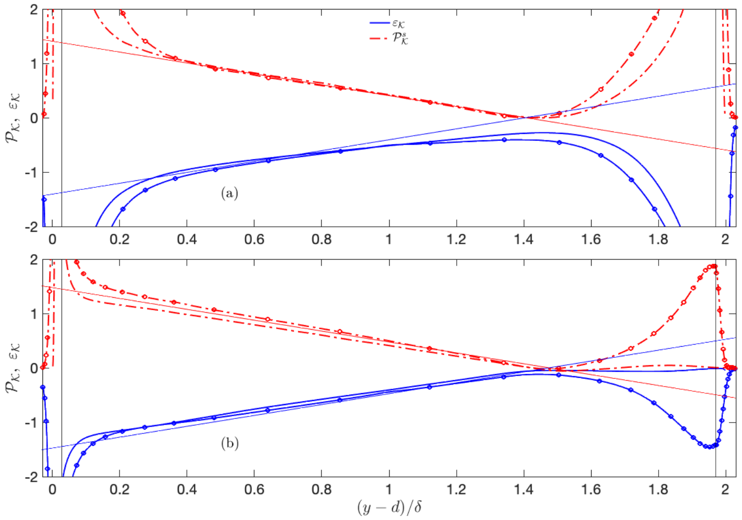

Figure 16: Production and dissipation of TKE, normalized by $(u^4_{\tau,avg}/\nu)(Ro_\tau/Re_\tau)$. (a) $Ro_b = 0.42$; (b) $Ro_b = 1.00$. Lines: smooth wall; lines with symbols: rough wall. The black line indicates the location of the roughness crest. The thin red and blue lines have a slope of -1 and +1, respectively.

case, which, in turn affect the production of $\left\langle \overline{u'u'} \right\rangle$ and TKE.

The production and dissipation of TKE are shown in Figure 16. They are normalized by $(u^4_{\tau,avg}/\nu)(Ro_\tau/Re_\tau)$. Brethouwer (2017) observes that these quantities are linear in the region in which $d\left\langle \overline{u} \right\rangle/dy = -2\Omega$, and that, if normalized by $(u^4_{\tau,avg}/\nu)(Ro_\tau/Re_\tau)$, the slope of the linear region is ± 1. This behaviour is affected, near the wall, by roughness: both production and dissipation depart from the linear behaviour further away from the wall, compared with the smooth-wall case. Since the extent of the linear region of $\left\langle \overline{u'v'} \right\rangle$ is unchanged by roughness (Figure 5(d)), this departure is due to differences in the slope of the mean velocity (Figure 3(a)).

4. Conclusions

We have performed direct numerical simulations of turbulent channel flows subjected to spanwise rotation, comparing smooth and rough surfaces. The Reynolds number, for the non-rotating case, is fairly high, $Re_\tau = 950$ and 1,500 for smooth and rough walls, respectively. This allows the fully rough regime to be achieved, while keeping blockage effects small (the roughness height is 4% of the channel half-height).

Roughness tends to destabilize the flow, and full relaminarization is not observed, even at the highest rotation rate; the velocity profiles is closer to the logarithmic behaviour on the stable side. On the unstable one, the downward shift (the roughness function) is observed, but the equivalent sandgrain height, k_s, is lower than in the non-rotating case. This difference is only partly due to the fact that for $Ro_b = 0.00$ the flow is fully rough, while in the other cases the roughness is transitional.

The destabilizing role played by the roughness is particularly evident on the stable, cyclonic, side of the channel. Significantly more energy is present in the v' and w' fluctuations, decreasing the flow anisotropy; this is similar to the non-rotating case. At the highest rotation rate examined, $Ro_b = 1.00$, when the wall is smooth the shear stress $\langle u'v' \rangle$ vanishes, while it remains significant on the rough wall. In the rotating case Taylor's similarity hypothesis only applies to the $\left\langle \overline{u'u'} \right\rangle$ stresses. Also, the region in which the velocity profile is linear becomes somewhat narrower, and roughness affects the equilibrium between production and dissipation of turbulent kinetic energy.

The anisotropy of the Reynolds stresses is decreased by roughness, on both stable and unstable sides. The Reynolds-stress anisotropy maps show that, on the stable side, turbulence is in the axisymmetric compression state in the roughness sublayer, and the axisymmetric expansion region is reduced, as previously observed by Busse and Sandham (2012). This behaviour is not altered qualitatively by rotation, although the axisymmetric expansion becomes stronger. On the unstable side the flow moves directly from the axisymmetric compression to the expansion state, independent of rotation.

The difference between the time-averaged and double-averaged velocity (the wake velocity $\widetilde{u}_i$) plays an important role in the dynamics of rough-wall flows. The dispersive stresses $\widetilde{u}_i \widetilde{u}_j$ are significantly reduced by rotation on the stable side, not on the unstable one. Their anisotropy is markedly different from that of the Reynolds stresses, remaining closer to the axisymmetric expansion state throughout the roughness sublayer. This behaviour is due to the channeling of the flow between roughness elements, and is not strongly affected by rotation.

Roughness changes the mechanisms of energy transfer between the various stress components. In smooth walls, on the unstable side the pressure-strain correlation redistributes energy from $\left\langle \overline{v'v'} \right\rangle$ to the other two normal stresses; the pressure diffusion, however, partially counteracts this effect, so that the combined effect of the pressure terms is to decrease $\left\langle \overline{u'u'} \right\rangle$ and increase $\left\langle \overline{w'w'} \right\rangle$. The effect of the pressure terms on $\left\langle \overline{v'v'} \right\rangle$ depends on the rotation rate, increasing it at low rotation, decreasing it at high rotations. On rough wall the pressure diffusion is negligible, and the pressure-strain correlation redistributes energy from $\left\langle \overline{u'u'} \right\rangle$ to $\left\langle \overline{v'v'} \right\rangle$ and $\left\langle \overline{w'w'} \right\rangle$ for $Ro_b = 0$ and 0.42, and from $\left\langle \overline{v'v'} \right\rangle$ to $\left\langle \overline{u'u'} \right\rangle$ and $\left\langle \overline{w'w'} \right\rangle$ for the highest rotation rate. The form-induced production is not negligible.

The wake field affects the $\left\langle \overline{u'v'} \right\rangle$ budget most significantly, especially on the stable side, where the magnitude of the form-induced production is comparable or larger than that of the other terms. Thus, it appears that the turbulence generation cycle, on the stable side, is initiated by the production due to the stationary wake fluctuations, which destabilize the flow, resulting in more significant shear stress. $\left\langle \overline{u'v'} \right\rangle$ in turn affects the production of $\left\langle \overline{u'u'} \right\rangle$. The $\left\langle \overline{v'v'} \right\rangle$ stresses receive energy from $\left\langle \overline{u'u'} \right\rangle$ through the action of the pressure-strain correlation, further increasing $\left\langle \overline{u'v'} \right\rangle$ through its shear production.

Two findings of this work may be important for industrial applications also: turbulence models for the Reynolds-Averaged Navier-Stokes equations usually model roughness by defining a virtual wall, where the velocity and eddy viscosity are non-zero; the transport equations for the turbulent quantities are then modified based on the equivalent sandgrain roughness k_s. Our work indicates that the relationship between roughness height and k_s must be modified. Furthermore, the details of the geometry are important, as the wake field causes additional production of the Reynolds shear stresses. It would be desirable to incorporate this effect into turbulence models. The decreased anisotropy due to roughness could be beneficial, from the modelling point of view, as eddy-viscosity models do not account for the flow anisotropy.

Acknowledgments

UP acknowledges the support from Hydro-Québec and the Natural Science and Engineering Research Council of Canada (NSERC) under the Collaborative Research and Development program (Grant No. CRDPJ 418786 - 11). The simulations were performed at the Centre for Advanced Computing, Queen's site. UP also acknowledges the support of the Canada Research Chair program.

References

del Álamo JC, Jiménez J, Zandonade P, Moser RD. Scaling of the energy spectra of turbulent channels. J Fluid Mech 2004;500:135–44. doi:`10.1017/S002211200300733X`.

Brethouwer G. Statistics and structure of spanwise rotating turbulent channel flow at moderate Reynolds numbers. J Fluid Mech 2017;828:424–58. doi:`10.1017/jfm.2017.526`.

Busse A, Sandham ND. Parametric forcing approach to rough-wall turbulent channel flow. J Fluid Mech 2012;712:169–202. doi:`10.1017/jfm.2012.408`.

Colebrook CF. Turbulent flow in pipes with particular reference to the transition region between smooth- and rough-pipe laws. J Inst Civ Eng 1939;11:133–56.

Durbin PA, Pettersson Reif BA. Statistical theory and modeling for turbulent flows. 2nd ed. Wiley, 2011.

Flack KA, Schultz MP, Connelly JS. Examination of a critical roughness height for outer layer similarity. Phys Fluids 2007;19:095104.

Grundestam O, Wallin S, Johansson AV. Direct numerical simulations of rotating turbulent channel flow. J Fluid Mech 2008;598:177–99. doi:`10.1017/S0022112007000122`.

Hoyas S, Jiménez J. Scaling of the velocity fluctuations in turbulent channels up to Re_τ=2003. Phys Fluids 2006;18:011702.

Jackson P. On the displacement height in the logarithmic velocity profile. J Fluid Mech 1981;111:15–-25.

Johnston JP, Halleen RM, Lezius RK. Effect of spanwise rotation on the structure of two-dimensional fully developed turbulent channel flow. J Fluid Mech 1972;56(03):533–57.

Kristoffersen R, Andersson HI. Direct simulations of low-Reynolds-number turbulent flow in a rotating channel. J Fluid Mech 1993;256:163–97.

Lamballais E, Lesieur M, Métais O. Effects of spanwise rotation on the vorticity straining in transitional and turbulent channel flows. Int J Heat Fluid Flow 1996;17:324–32.

Lamballais E, Métais O, Lesieur M. Spectral-Dynamic Model for Large-Eddy Simulations of Turbulent Rotating Channel Flow. Theor Comput Fluid Dyn 1998;12(3):149–77.

Lumley JL. Computational modelling of turbulent flows. Adv Appl Mech 1978;18:123–76.

Maciel Y, Picard D, Yan G, Dumas G, Gleyzes C. Fully developed turbulent channel flow subject to system rotation. *AIAA Paper 2003-4153*; 2003.

Mignot E, Barthelemy E, Hurter D. Double-averaging analysis and local flow characterization of near-bed turbulence in gravel-bed channel flows. J Fluid Mech 2009;618:279–-303. doi:`10.1017/S0022112008004643`.

Nakabayashi K, Kitoh O. Low Reynolds number fully developed two-dimensional turbulent channel flow with system rotation. J Fluid Mech 1996;315(1):1–29.

Nakabayashi K, Kitoh O. Turbulence characteristics of two-dimensional channel flow with system rotation. J Fluid Mech 2005;528:355–77. doi:`10.1017/S0022112004002939`.

Narasimhamurthy VD, Andersson HI. Turbulence statistics in a rotating ribbed channel. Int J Heat Fluid Flow 2015;51:20–41. doi:`10.1016/j.ijheatfluidflow.2014.10.008`.

Nikora V, McEwan I, McLean S, Coleman S, Pokrajac D, Walters R. Double-averaging concept for rough-bed open-channel and overland flows: theoretical background. J Hydr Engng 2007;133(8):873–83. doi:`10.1061/(ASCE)0733-9429(2007)133:8(873)`.

Perry AE, Joubert PN. Rough wall turbulent boundary layers. J Fluid Mech 1969;37(02):193–211.

Pope SB. Turbulent Flows. Cambridge, U.K.: Cambridge Univ. Press, 2000.

Raupach MR, Antonia RA, Rajagopalan S. Rough-wall boundary layers. App Mech Rev 1991;44(1):1–25.

Scotti A. Direct numerical simulation of turbulent channel flows with boundary roughened with virtual sandpaper. Phys Fluids 2006;18:031701–1. doi:`10.1063/1.2183806`.

Tafti DK, Vanka SP. A numerical study of the effects of spanwise rotation on turbulent channel flow. Phys Fluids A 1991;3(4):642–56.

Wu W, Piomelli U. Effects of surface roughness on a separating turbulent boundary layer. J Fluid Mech 2018;841:552–80. doi:`10.1017/jfm.2018.101`.

Xia Z, Shi Y, Chen S. Direct numerical simulation of turbulent channel flow with spanwise rotation. J Fluid Mech 2016;788:42–56. doi:`10.1017/jfm.2015.717`.

Yuan J, Piomelli U. Numerical simulations of sink-flow boundary layers over rough surfaces. Phys Fluids 2014a;26:015113–1. doi:`10.1063/1.4862672`.

Yuan J, Piomelli U. Roughness effects on the Reynolds stress budgets in near-wall turbulence. J Fluid Mech 2014b;760:R1–1. doi:`10.1017/jfm.2014.608`.

Yuan J, Piomelli U. Numerical simulation of a spatially developing accelerating boundary layer over roughness. J Fluid Mech 2015;780:192–214. doi:`10.1017/jfm.2015.437`.

Response to Reviewe 1

We thank the Reviewer for their comments. The changes made in response to thir comments are highlighted in red, and listed below.

1. *In Fig.5(d), the Reynolds shear stress profiles away from the rough surface in case* $Ro = 0.0$ *do not seem to follow a linear line despite the fact that the dispersive shear stress is negligibly small in the region. Does the total shear stress (the Reynolds shear stress, dispersive shear stress, and viscous shear stress) profile shows a linear profile with respect to* y/δ*?*

   The total shear stress is indeed linear if the dispersive and viscous stresses are included. The dispersive stresses are non-zero in the channel interior. This may be due to large-scale motions that have been observed by several researchers, in flows over smooth and rough surfaces (**???**). This is now explained in the text.

2. *In the bottom of page 12, the authors state that the flow is preferentially moving in the channels between roughness elements. Along these channels, large value of* $\widetilde{u}$ *tend to be associated with larger values of* $\widetilde{w}$ *than* $\widetilde{v}$*. This is not clear to me. Fig.10 (a) and (b) shows that the correlation between*$\widetilde{u}$ *and* $\widetilde{v}$ *is more significant than that between* $\widetilde{u}$ *and* $\widetilde{w}$*; thus indicating that* $\widetilde{u}$ *tend to be associated with larger values of* $\widetilde{v}$*. In my opinion, the explanation would be clearer if you could discuss with the visualization of the mean velocity distribution in the x-z plane below the roughness crest.*

   We have added two Figures (Figs 10 and 12) and expanded significantly the explanation (pages 13 and following).

3. *The double-averaged Reynolds stress equation may include some typos....*

   The equation has been corrected.

4. *Basically, a diffusion term should be zero when integrated over the entire domain; however, the integral of the pressure diffusion in Fig.12 does not seem to be zero.*

   The diffusion term does indeed integrate to zero. Through most of the channel ($0.15 < y < 0.85$) the diffusion term is negative, although very small (one or two orders of magnitude smaller than the peak value).

5. All the typos pointed out as ”Minor points” have been corrected.

Response to Reviewer 2

We thank the Reviewer for their comments. There is a problem relating our findings to those of Narasimhamurthy and Andersson (2015): our focus is on the differences between rough and smooth cases. In their paper, on the other hand, they discuss mainly the effect of Ro on the flow features, and the spatial development of the flow, but do not compare their results to a smooth-wall case. Consider, for instance, the reduction in the flow anisotropy that the Reviewer mentions. In our paper, we compare the anisotropy of the smooth and rough cases. Narasimhamurthy and Andersson (2015), on the other hand, focus on the effects of rotation rate on the Reynolds stresses: On page 36 they discuss the differences between the statistics near the rib and in the channel center, but never discuss the effect of the ribs on the flow anisotropy, or compare to a smooth case.

Nonetheless, we have tried to insert references to their work wherever it appeared justified (they are highlighted in blue in the paper).